



# Solar Energetic Particle Events with Extremely High $^3\text{He}$ Content Observed by Solar Orbiter

A. Kouloumvakos<sup>1</sup> , G. M. Mason<sup>1</sup> , G. C. Ho<sup>2</sup> , R. C. Allen<sup>2</sup> , J. Rodriguez-Pacheco<sup>3</sup> , and R. F. Wimmer-Schweingruber<sup>4</sup>

<sup>1</sup> The Johns Hopkins University Applied Physics Laboratory, 11101 Johns Hopkins Road, Laurel, MD 20723, USA

<sup>2</sup> Southwest Research Institute, 6220 Culebra Road, San Antonio, TX 78238, USA

<sup>3</sup> Universidad de Alcalá, Space Research Group, 28805 Alcalá de Henares, Spain

<sup>4</sup> Institute of Experimental and Applied Physics, Christian-ALbrechts-University Kiel, 24118 Kiel, Germany

Received 2024 November 25; revised 2025 February 24; accepted 2025 February 25; published 2025 April 7

## Abstract

We performed a survey of  $^3\text{He}$ -rich events using observations from the Suprathermal Ion Spectrograph on the Solar Orbiter mission from 2020 to 2024. We identified 57  $^3\text{He}$ -rich events, each showing clear  $^3\text{He}$  enhancements above the background and  $^3\text{He}/^4\text{He}$  abundance ratios greater than 1 in at least one energy channel in the range from 193.2 keV nucleon<sup>-1</sup> to 8.74 MeV nucleon<sup>-1</sup>. The analysis of the events' abundance ratios shows characteristics of impulsive solar energetic particle events with  $^3\text{He}/^4\text{He} \sim 3.1$  and  $\text{Fe}/\text{O} \sim 1.3$ . We observe an energy dependence in the  $^3\text{He}/^4\text{He}$  ratio, which increases with energy, while the  $\text{Fe}/\text{O}$  ratios are almost constant with energy. We also found that six events in our list have extremely high  $^3\text{He}$  content (e.g.,  $^3\text{He}/\text{C-Fe}$  ratios in the range 25–62). These events show curved  $^3\text{He}$  and heavy nuclei spectra that roll over at higher energies and flatten toward low energy. Their spectral forms can be reasonably fit with simple exponentials with a  $^3\text{He}$  rollover energy in the range of a few hundred keV per nucleon and a C–Fe rollover energy  $\sim 2$ –3 times lower. The differences in spectral rollover energy lead to a strong energy dependence of the ratio  $^3\text{He}/\text{C-Fe}$ , rising sharply with energy. We conclude that the features of these events with extremely high  $^3\text{He}$  content have a reasonable likelihood of depicting the initial acceleration process, which is driven by magnetic reconnection in flaring loops near the solar surface.

*Unified Astronomy Thesaurus concepts:* [Solar physics \(1476\)](#); [Solar particle emission \(1517\)](#); [Solar abundances \(1474\)](#)

## 1. Introduction

The abundance of elements and isotopes in solar energetic particles (SEPs) has been extensively used as an indicator of the acceleration mechanisms involved and the transport conditions in the inner heliosphere. One aspect of particular interest is the isotopic composition of SEPs, including isotopes such as  $^3\text{He}$ . The preferential enrichment of  $^3\text{He}$  during solar events indicates the involvement of specific mechanisms, such as magnetic reconnection, which can selectively enhance the rare He isotope  $^3\text{He}$  over the usually much more abundant  $^4\text{He}$ . The origins of this preferential acceleration are not yet well understood and remain among the main unresolved issues in solar physics (e.g., see reviews by G. M. Mason 2007; R. Bučík 2020; D. V. Reames 2021).

From the first observation of  $^3\text{He}$ -rich SEP events by K. C. Hsieh & J. A. Simpson (1970) to today, there has been a significant effort in the field of SEP acceleration, both observational and theoretical, to better understand the production of  $^3\text{He}$ -rich events in the solar corona. Initially, the presence of  $^3\text{He}$  in some events was attributed to nuclear reactions in solar flares (see, e.g., V. K. Balasubrahmanyam & A. T. Serlemitsos 1974; J. D. Anglin 1975); however, this scenario was quickly abandoned, since no evidence of other nuclear reaction products ( $^2\text{H}$  or  $^3\text{H}$ ) has been observed (J. D. Anglin 1975; A. T. Serlemitsos & V. K. Balasubrahmanyam 1975). Later studies suggested that a stochastic interaction

of particles with cascading waves (stochastic acceleration through plasma wave–particle resonance) could play a key role in  $^3\text{He}$  and heavy ion acceleration (e.g., see review papers by L. G. Kocharov & G. E. Kocharov 1984; J. A. Miller 1998, 2000). These waves could be generated at a frequency close to  $\omega(^3\text{He})$  by several different processes such as electric currents (L. A. Fisk 1978), electron beams (M. Temerin & I. Roth 1992), or turbulent plasma waves (S. Liu et al. 2004, 2006).

L. A. Fisk (1978) proposed that current-driven electrostatic  $^4\text{He}$  cyclotron waves could preferentially accelerate  $^3\text{He}$  and heavy ions by the first and second harmonic resonance, respectively. Similarly, current-driven electrostatic proton cyclotron waves would have the same effect (T. X. Zhang 1995, 1999, 2003; T. M. Li et al. 2021). Electron beams can also excite plasma waves such as Langmuir waves, electrostatic waves, and electromagnetic ion cyclotron waves (e.g., T. H. Stix 1992; S. P. Gary 1993). M. Temerin & I. Roth (1992) proposed that flare-accelerated electron beams could generate electromagnetic proton cyclotron waves that could selectively accelerate  $^3\text{He}$  and heavy ions (see also I. Roth & M. Temerin 1997; A. Broaden et al. 2013). Several other mechanisms have also been proposed (e.g., I. Roth 2006; J. F. Drake et al. 2009), including turbulent plasma waves (S. Liu et al. 2004, 2006), electromagnetic plasma waves driven by the electron firehose instability (G. Paesold et al. 2003), and ion beam instabilities (A. Fitzmaurice et al. 2024).

The characteristics of SEP composition and energy spectra are important properties that can hint at the acceleration processes involved. Previous studies have shown large variability in the elemental abundances and spectral shapes of



Original content from this work may be used under the terms of the [Creative Commons Attribution 4.0 licence](#). Any further distribution of this work must maintain attribution to the author(s) and the title of the work, journal citation and DOI.

$^3\text{He}$ -rich events (G. M. Mason et al. 2000, 2002). The  $^3\text{He}/^4\text{He}$  abundance ratio is generally observed to lie between 0.01 and 10 and correlates weakly with the Fe/O ratio, as shown in a large statistical survey by S. T. Hart et al. (2022). The spectral forms in  $^3\text{He}$ -rich events are generally observed to be a power law or a power law with an exponential rollover in the observed energy range (G. M. Mason et al. 2002; G. M. Mason 2007). Notably, certain events exhibit distinct spectral shapes among different species, as highlighted by G. M. Mason et al. (2002, 2016). This feature complicates the interpretation of these cases.

Solar Orbiter (D. Müller et al. 2020) observations provide an unprecedented opportunity to study  $^3\text{He}$ -rich events. In this study, we used data from the Suprathermal Ion Spectrograph (SIS) instrument, which is part of the Energetic Particle Detector (J. Rodríguez-Pacheco et al. 2020; R. F. Wimmer-Schweingruber et al. 2021) instrument suite on board the Solar Orbiter mission. The proximity of the spacecraft to the Sun (from 0.3 to 1.0 au) and the very high mass resolution of SIS allows us to examine the properties of small  $^3\text{He}$ -rich events that otherwise are difficult to study because their fluxes are close to the statistical uncertainties from observations at 1 au. For example, G. M. Mason et al. (2023a) showed that small flaring loops only visible in EUV can produce small  $^3\text{He}$ -rich injections even without any X-ray flare signatures. Moreover, SIS observations have shown the nearly continuous presence of  $^3\text{He}$  for many days that is related to solar activity near active regions where the spacecraft is magnetically connected during the analyzed time periods (R. Bučík et al. 2021; A. Kouloumvakos et al. 2023). SIS has also observed events with multiple  $^3\text{He}$  injections over a short period of time (R. Bučík et al. 2023), some of which also show multiple ion flux dropouts (G. C. Ho et al. 2022). In a recent study, G. M. Mason et al. (2024) analyzed  $^3\text{He}$ -rich events observed from SIS, focusing on events with curved  $^3\text{He}$  and Fe spectra. That study showed that the spectral shapes and intensities of  $^3\text{He}$  and Fe are similar and that the  $^3\text{He}$  spectrum nearly coincides with the Fe spectrum if it is shifted to lower energy, suggesting a close connection.

In our study, we have explored  $^3\text{He}$ -rich events observed by SIS with extremely high  $^3\text{He}$  content. In the first part of the study, we select events with  $^3\text{He}/^4\text{He} > 1$ , which represents a striking deviation from the isotopic composition of the solar wind and the solar atmosphere, where  $^3\text{He}$  is typically much less abundant. These type of events, with a large relative abundance of  $^3\text{He}$ , have been observed since the 1970s (see T. L. Garrard et al. 1973; V. K. Balasubrahmanyam & A. T. Serlemitsos 1974; J. D. Anglin 1975; A. T. Serlemitsos & V. K. Balasubrahmanyam 1975). The analysis of these events can provide further insights into particle acceleration mechanisms since their spectra are as close as possible to those from the primary acceleration event, before possible later processing by reacceleration or other effects such as propagation. In Section 2, we present the list of events from our survey, and then we analyze the fluence and abundance ratio characteristics of our sample. In Section 3, we continue with the analysis of a particular class of events that show extremely high  $^3\text{He}$  content compared to heavy ions in the range C–Fe. Finally, in Section 4, we discuss and summarize our findings.

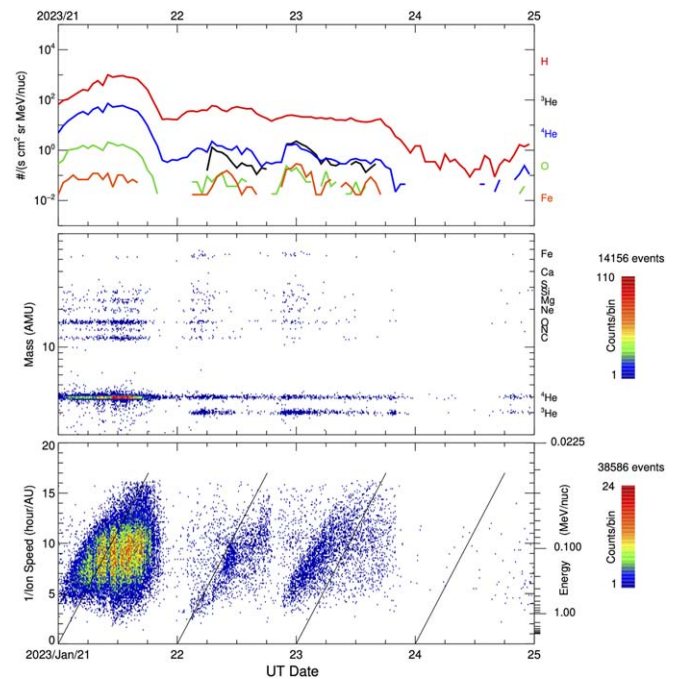


**Figure 1.** SIS observations for the 2023 January 22  $^3\text{He}$ -rich events. The top panel shows a time intensity plot of  $\sim 0.23$ – $0.32$  MeV nucleon $^{-1}$  ions. The middle panel shows the mass spectrogram for heavy ions (helium and heavier) in  $0.3$ – $10$  MeV nucleon $^{-1}$ . The bottom panel shows the inverse-velocity measurements of heavy ions (C–Fe).

## 2. Observations and Data Analysis

### 2.1. Instrumentation

In this study, we employed energetic particle data from the SIS instrument on board Solar Orbiter. SIS is a high-resolution mass spectrometer that measures both elemental and isotopic ion composition in the energy range of  $\sim 50$  keV nucleon $^{-1}$  to  $\sim 10$  MeV nucleon $^{-1}$ , with a very high mass resolution ( $\sigma_m/m \sim 0.02$ ), low background, and a geometry factor of  $\sim 0.38$  cm $^2$  sr. SIS has two telescopes that point at different looking directions (J. Rodríguez-Pacheco et al. 2020). One telescope points at  $30^\circ$  (SIS-a; sunward telescope) and the other at  $160^\circ$  (SIS-b; antisunward telescope) to the west of the spacecraft–Sun line. SIS-a is primarily used in the analysis of the SEP characteristics, while SIS-b is used to explore the anisotropy of the events.

### 2.2. A Survey of $^3\text{He}/^4\text{He} > 1$ Events

We performed a survey of  $^3\text{He}$ -rich events using SIS observations from 2020 April, when SIS was first commissioned, through 2024 May. This time interval covers seven complete orbits of Solar Orbiter around the Sun. We searched for SEP events in SIS data with  $^3\text{He}/^4\text{He} > 1$  in at least one of the 12 energy channels from  $193.2$  keV nucleon $^{-1}$  to  $8.74$  MeV nucleon $^{-1}$ . For this, we used publicly available SIS data provided from the Solar Orbiter Archive.<sup>5</sup> First, we resampled the time series of  $^3\text{He}$  and  $^4\text{He}$  fluxes to a 3 hr cadence and calculated the  $^3\text{He}/^4\text{He}$  ratio. Subsequently, we searched for time periods where the ratio was greater than unity in at least one energy channel and the  $^3\text{He}$  fluxes exceeded  $3\sigma$  of the background for at least two consecutive points. For each time period, we registered individual  $^3\text{He}$ -rich SEP events with

<sup>5</sup> <https://soar.esac.esa.int/>

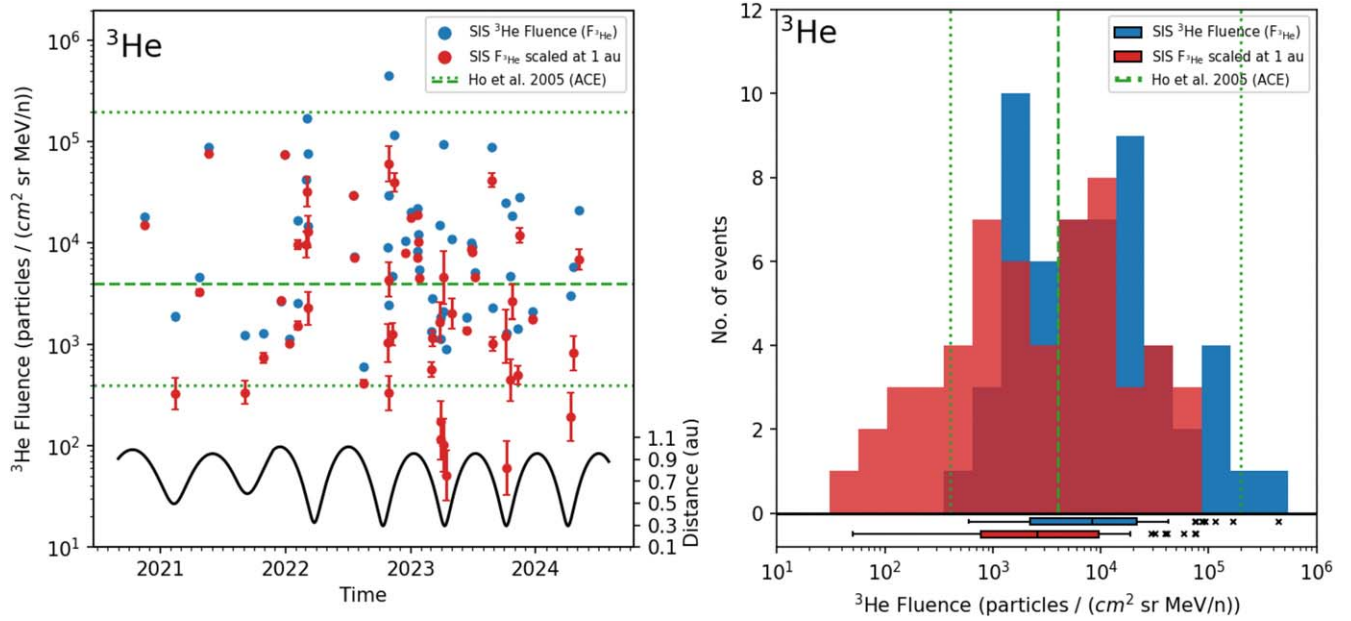


**Figure 2.** Results from the analysis of  $^3\text{He}$  fluences. The left panel shows the  $^3\text{He}$  fluence values (blue symbols) for each event in our list, plotted vs. time. The red symbols show the scaled fluence calculated at 1 au, assuming a  $1/R^{2.5}$  dependence for the middle points and  $1/R^2$  or  $1/R^3$  for the vertical error bars. The Solar Orbiter's radial distance is also shown at the bottom of this panel (black line). The right panel shows the distributions of  $^3\text{He}$  fluence (blue) and scaled  $^3\text{He}$  fluence at 1 au (red). At the bottom part of this panel, we show the box plots of the two distributions showing the median, interquartile range, whiskers, and outliers. Note that the outliers shown in the box plots are not the same for the two distributions. The dashed green lines in each panel show the mean and upper-/lower-limit fluence values determined in a large survey of  $^3\text{He}$ -rich events by G. C. Ho et al. (2005).

$^3\text{He}/^4\text{He} > 1$ . Figure 1 shows SIS observations from 2023 January 21 to 24. During this period, for example, two  $^3\text{He}$ -rich SEP events with  $^3\text{He}/^4\text{He} > 1$  were found. Finally, after a careful inspection of daily He mass spectrograms, we identified and included another five small events (#5, #18, #24, #39, and #40) that had been missed in our initial selection because of the long averaging of the time series in the above process. We also verified that none of the identified intervals exhibited significant spillover of  $^4\text{He}$  into the  $^3\text{He}$  mass range.

From this survey, we found 57 events that we list in Table A1. For each event in our survey, we list in column (2) the date of the event and in column (3) the approximate time when the SEP intensities started to be elevated (e.g., the onset time). In column (4), we list the heliocentric distance of the spacecraft at the onset time. About 37% of the events (21 cases) were observed when Solar Orbiter was located at a distance below 0.5 au. Columns (5) and (6) list the  $^3\text{He}$  and  $^4\text{He}$  fluences (in particles/(cm<sup>2</sup> sr MeV nucleon<sup>-1</sup>)), respectively, calculated at  $\sim 0.39$  MeV nucleon<sup>-1</sup>. Columns (7)–(12) list the  $^3\text{He}/^4\text{He}$  and Fe/O abundance ratios calculated either at  $\sim 0.39$  MeV nucleon<sup>-1</sup> or the maximum ratios in the full spectrum energy range. Column (13) lists the maximum  $^3\text{He}/\text{H}$  ratios.

### 2.3. Fluence Characteristics

For each event, we calculated the  $^3\text{He}$  and  $^4\text{He}$  fluences for the full energy range covered by SIS. Moreover, since each event was observed at different heliocentric distances, we calculated a scaled fluence ( $F'$ ) at 1 au to make the results intercomparable and relatable to past studies at 1 au. For this calculation, we assumed that the radial dependence of  $F$  follows an inverse power law of distance such that  $F' = F * R^a$ , where  $R$  is the heliocentric distance of the

spacecraft and the exponent  $a = -2.5$  (e.g., D. Lario et al. 2013; L. Rodríguez-García et al. 2023).

Figure 2 shows the  $^3\text{He}$  fluences at  $\sim 0.39$  MeV nucleon<sup>-1</sup> (left panel) for each event and the distributions of fluence values (right panel). From the left panel of Figure 2, we observe significant event-to-event variability in the calculated fluences. Specifically, we found that the fluences range from  $\sim 150$  to  $\sim 4 \times 10^5$  particles/(cm<sup>2</sup> sr MeV nucleon<sup>-1</sup>). When scaling the  $^3\text{He}$  fluences to 1 au, we see that many of the events in our sample have very low values. In some cases, we found that the scaled fluences are lower than  $3 \times 10^2$  particles/(cm<sup>2</sup> sr MeV nucleon<sup>-1</sup>), which is a lower limit reported in previous surveys (e.g., G. C. Ho et al. 2005). Many of the events in this survey would be barely detectable by current instruments at 1 au. However, close to the Sun, their measured fluence from SIS is more than an order of magnitude higher, which makes it possible to study their characteristics with greater accuracy. On the other hand, for the largest  $^3\text{He}$ -rich events in this survey, we found that their scaled  $^3\text{He}$  fluence at 1 au does not exceed the upper limit of  $10^5$  particles/(cm<sup>2</sup> sr MeV nucleon<sup>-1</sup>), as reported by G. C. Ho et al. (2005) in their survey.

From the distribution characteristics of  $^3\text{He}$  fluences, we found that half of the events are distributed between  $\sim 2.2 \times 10^3$  and  $2.2 \times 10^4$  particles/(cm<sup>2</sup> sr MeV nucleon<sup>-1</sup>) (from the first and third quartiles). The  $F_{^3\text{He}}$  distribution has a median of  $\sim 8.4 \times 10^3$  particles/(cm<sup>2</sup> sr MeV nucleon<sup>-1</sup>) (mean:  $\sim 29.4 \times 10^3$ ) and exhibits characteristics of a lognormal distribution similar to what has been reported in previous surveys, such as in G. C. Ho et al. (2005).

### 2.4. Abundance Ratios

From the  $^3\text{He}$  and  $^4\text{He}$  fluences, we calculated the  $^3\text{He}/^4\text{He}$  abundance ratios. Figure 3 (top panel) shows for each event



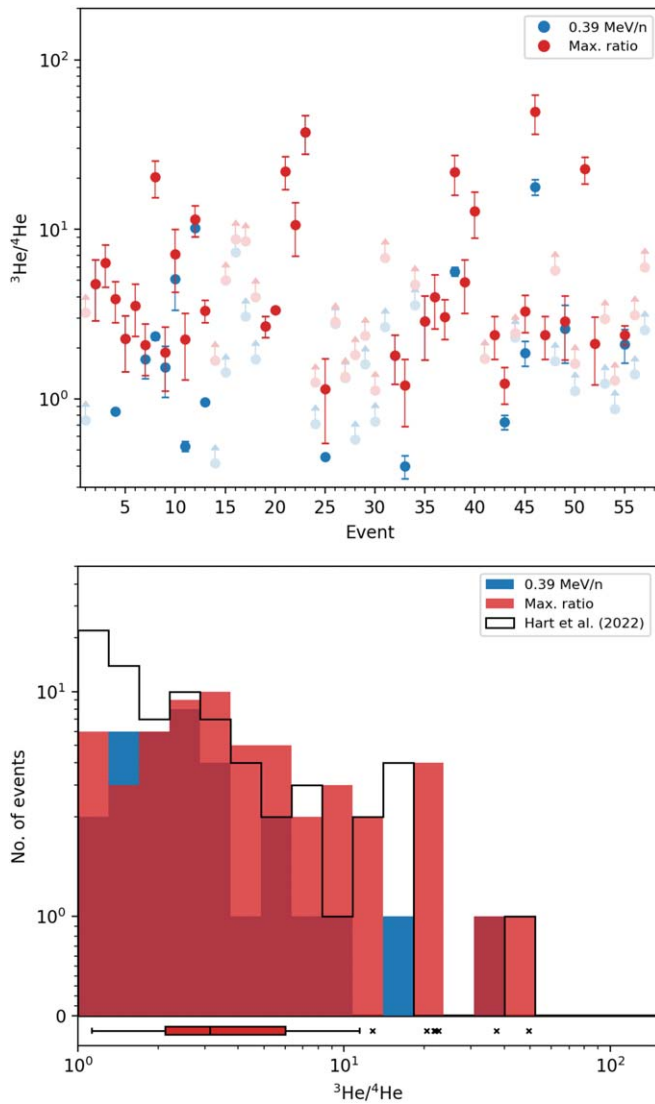


**Figure 3.** Results from the analysis of  ${}^3\text{He}/{}^4\text{He}$  abundance ratios. The top panel shows the  ${}^3\text{He}/{}^4\text{He}$  abundance ratio for each event. The blue symbols show the abundance ratio at a specific energy (0.39 MeV nucleon $^{-1}$ ), and the red markers show the maximum ratio observed across the entire energy spectrum for each event. The lower limits show events where the  ${}^4\text{He}$  did not show a large ( $\sim 10\times$ ) increase over the existing background from previous SEP events. The bottom panel shows the distribution of  ${}^3\text{He}/{}^4\text{He}$  abundance ratio values. The black line shows the distribution of  ${}^3\text{He}/{}^4\text{He}$  abundance ratios from the survey of  ${}^3\text{He}$ -rich events by S. T. Hart et al. (2022; see text for details).

the maximum  ${}^3\text{He}/{}^4\text{He}$  abundance ratios considering the full energy range (red symbols) and the  ${}^3\text{He}/{}^4\text{He}$  ratio at  $\sim 0.39^6$  MeV nucleon $^{-1}$  (blue). It is worth noting that during this analysis, we found many cases where the  ${}^4\text{He}$  did not show a large ( $\sim 10\times$ ) increase over the existing background from previous SEP events. These events are marked as lower limits (faded colored markers and lower-limit arrows) in Figure 3.

From the analysis of the maximum  ${}^3\text{He}/{}^4\text{He}$  ratios, we found that some events exhibit very high values. There are nine events where the maximum  ${}^3\text{He}/{}^4\text{He}$  ratio exceeds 10 (#8, 12, 21, 22, 23, 38, 40, 46, and 51). In Figure 3 (top panel), we see that the maximum  ${}^3\text{He}/{}^4\text{He}$  abundance ratios are usually

<sup>6</sup> We selected this energy channel to be comparable with previous statistical analysis.

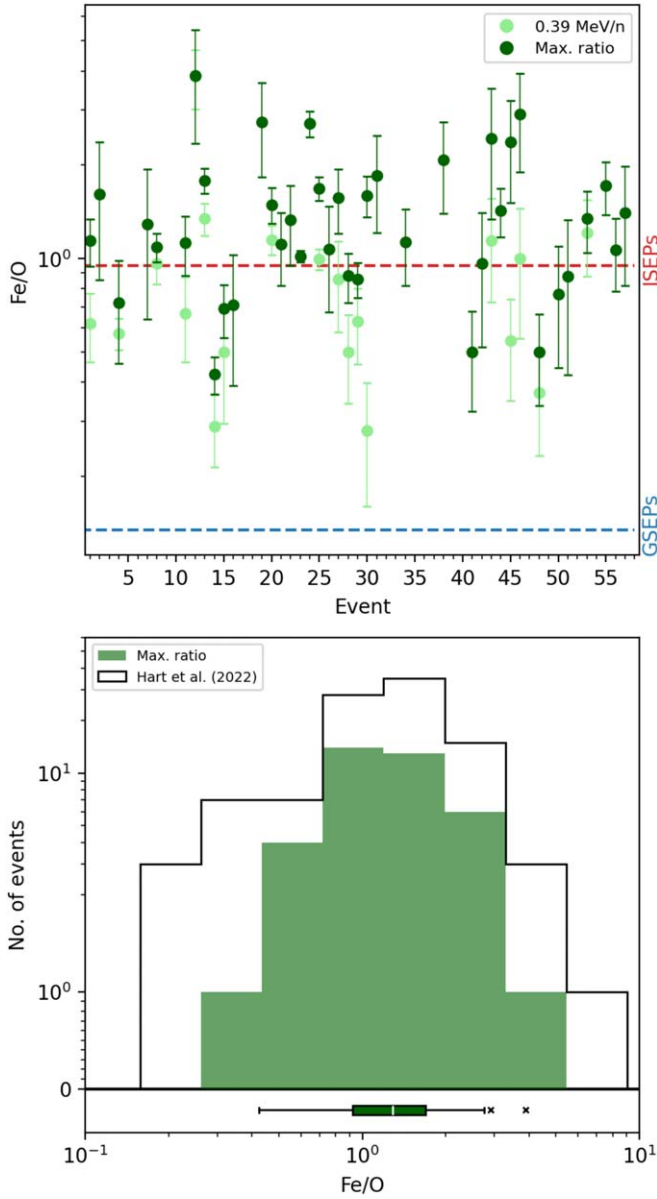
different from the ratios calculated at  $\sim 0.39$  MeV nucleon $^{-1}$ . In almost half of the cases, this difference exceeds a factor of 1.5. This indicates an energy dependence in the ratios for many events, as we will show later in the analysis. Typically, the  ${}^3\text{He}/{}^4\text{He}$  ratio is maximum at  $\sim 0.55$  MeV nucleon $^{-1}$ .

Figure 3 (bottom panel) shows the distribution of  ${}^3\text{He}/{}^4\text{He}$  abundance ratios. We found a median value of 3.1 (mean: 6.5) for the distribution of the maximum  ${}^3\text{He}/{}^4\text{He}$  ratios and of 1.7 (mean: 3.4) for the distribution of  ${}^3\text{He}/{}^4\text{He}$  at  $\sim 0.39$  MeV nucleon $^{-1}$ . Half of the events have maximum  ${}^3\text{He}/{}^4\text{He}$  ratios between 2.1 and 6.1. In the same panel, we also show the distribution of  ${}^3\text{He}/{}^4\text{He}$  ratios at 0.39 MeV nucleon $^{-1}$  from the multispacecraft survey of  ${}^3\text{He}$ -rich events conducted by S. T. Hart et al. (2022) using data from the Advanced Composition Explorer (ACE) and the Solar Terrestrial Observatory spacecraft. Here, we show only events observed by ACE with  ${}^3\text{He}/{}^4\text{He} > 1$ . Comparing our distribution of  ${}^3\text{He}/{}^4\text{He}$  ratios with that from the S. T. Hart et al. (2022) survey, we observe similar characteristics. Note, however, that the selection criteria between our study and S. T. Hart et al. (2022) are different, as their sample includes all  ${}^3\text{He}$ -rich SEP events observed by the two spacecraft, without any further selection of events based on the  ${}^3\text{He}/{}^4\text{He}$  ratios.

Figure 4 shows the results of the Fe/O abundance ratio analysis, similar to what we presented in Figure 3 for the  ${}^3\text{He}/{}^4\text{He}$ . From this analysis, we found that all events have a high Fe/O ratio, well above the gradual SEP average from Table 3 in M. I. Desai et al. (2006; see also D. V. Reames 1995; G. M. Mason et al. 2004). In 28 events, we found that the maximum Fe/O abundance ratio is greater than 1. Clearly, the results for the Fe/O ratios indicate that the events in our list exhibit characteristics similar to “impulsive” SEP events. From the distribution of the maximum Fe/O ratio values (bottom panel of Figure 4), we found a median of 1.3 (mean: 1.4). The Fe/O distribution shows similar characteristics to that of  ${}^3\text{He}$ -rich events from previous surveys (e.g., centered around 1), despite the fact that the selection criteria in our survey only include events with the largest  ${}^3\text{He}/{}^4\text{He}$  abundances. We show, for example, the corresponding distribution from the S. T. Hart et al. (2022) survey in the bottom panel of Figure 4. Lastly, it is worth noting that our selection criteria required only that  ${}^3\text{He}/{}^4\text{He} > 1$ ; therefore, the high  ${}^3\text{He}/{}^4\text{He}$  ratios shown in Figure 3 are expected. However, the high Fe/O ratio shown here (e.g., see Figure 4) was not part of the selection criteria of this survey.

We also examined the  ${}^3\text{He}/\text{H}$  abundance ratio; however, in most cases, the background H fluxes made it difficult to further explore its characteristics. Nevertheless, considering that  ${}^3\text{He}/\text{H} \ll 10^{-4}$  in the solar wind, we found that many events exhibit very high to extremely high  ${}^3\text{He}/\text{H}$  ratios. Half of the events show ratios between  $10^{-2}$  and 0.5, and the  ${}^3\text{He}/\text{H}$  distribution has a median of 0.2 (mean: 0.5). Interestingly, there are eight events (#20–23, 37, 38, 46, and 51) where  ${}^3\text{He}/\text{H} > 1$ , and in one extreme case (#23), the  ${}^3\text{He}$  is enhanced by a factor of about 8 compared to H.

We further analyzed the  ${}^3\text{He}/{}^4\text{He}$  and Fe/O abundance ratios as a function of energy. Figure 5 shows the results of this analysis separating the events into three groups based on the  ${}^3\text{He}/{}^4\text{He}$  ratio. The edges for each group were chosen in a way that each contains approximately the same number of events. The resulting three groups shown in Figure 5 have  ${}^3\text{He}/{}^4\text{He} < 2.5$  (squares),  $2.5 \leq {}^3\text{He}/{}^4\text{He} < 5$  (triangles), and



**Figure 4.** Similar to Figure 3, the two panels show the Fe/O (green) abundance ratios for each event (top panel) and the distribution of the ratio values (bottom panel). In the top panel, the horizontal lines mark characteristic values for Fe/O abundance ratios for gradual and impulsive events from M. I. Desai et al. (2006; their Table 3). The black line shows the distribution of Fe/O abundance ratios from the S. T. Hart et al. (2022) survey (see text for details).

$^3\text{He}/^4\text{He} \geq 5$  (circles). For  $^3\text{He}/^4\text{He}$ , we observe that in all cases, the ratio increases with increasing energy. For events with  $^3\text{He}/^4\text{He} \geq 5$ , we found that the  $^3\text{He}/^4\text{He}$  ratio is strongly energy-dependent, whereas for the other two groups ( $^3\text{He}/^4\text{He} < 2.5$  and  $2.5 \leq ^3\text{He}/^4\text{He} < 5$ ), the ratio flattens (becomes constant) above  $\sim 0.3 \text{ MeV nucleon}^{-1}$ . The maximum of  $^3\text{He}/^4\text{He}$  at  $\sim 0.55 \text{ MeV nucleon}^{-1}$  mentioned earlier can be seen to be the peak of a broad distribution. For the Fe/O ratio, we see small differences in ratios with energies that are within the statistical uncertainty.

Figure 6 shows the heavy ion abundances normalized to  $^3\text{He}$  at  $\sim 0.19 \text{ MeV nucleon}^{-1}$  for events with extremely high  $^3\text{He}/^4\text{He}$  ratios ( $\geq 10$ ). These ratios are also compared with the ratios from all the other events in the list. This is shown in Figure 6 with the black filled markers. A first remark from this

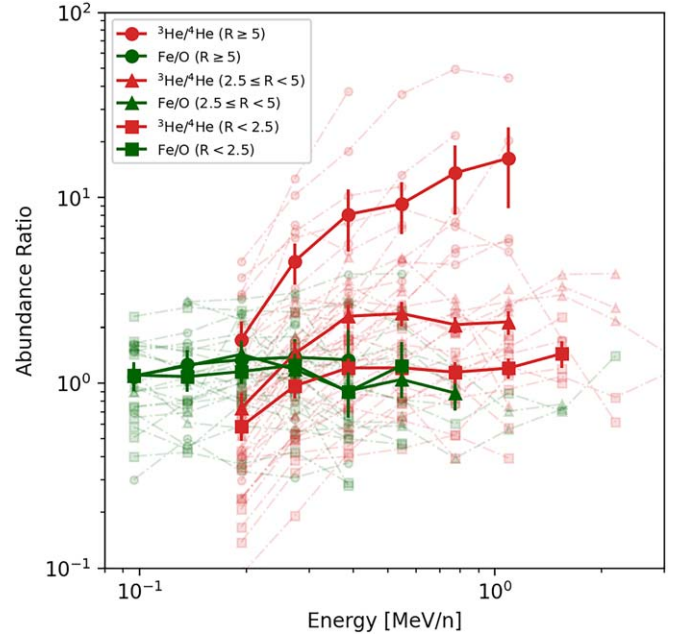


**Figure 5.** Abundance ratios of  $^3\text{He}/^4\text{He}$  (red markers) and Fe/O (green markers) as a function of energy. The events have been separated into three different groups with ratios  $^3\text{He}/^4\text{He} < 2.5$  (squares),  $2.5 \leq ^3\text{He}/^4\text{He} < 5$  (triangles), and  $^3\text{He}/^4\text{He} \geq 5$  (circles). The darker colored markers depict the mean of the abundance ratios at each energy, and the faded markers show the ratios for each event separately. The plotted uncertainties are calculated from the  $1\sigma$  standard error of the mean.

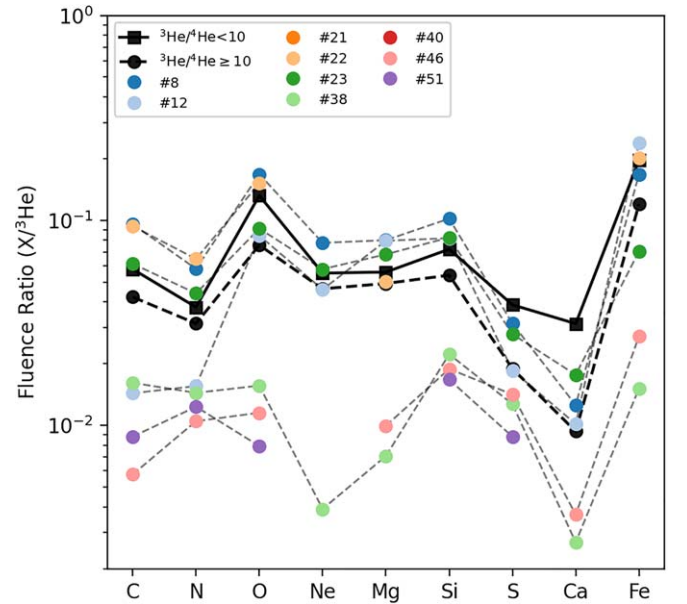


**Figure 6.** Heavy ion abundances normalized to  $^3\text{He}$  at  $\sim 0.19 \text{ MeV nucleon}^{-1}$  for events with  $^3\text{He}/^4\text{He} \geq 10$  ratios (colored circles). The mean values of the normalized heavy ion abundances for all the events with  $^3\text{He}/^4\text{He}$  ratios  $< 10$  are shown with black squares and for ratios  $\geq 10$  with circles.

analysis is that the heavy ion abundances normalized to  $^3\text{He}$  at  $\sim 0.19 \text{ MeV nucleon}^{-1}$  for events with extremely high  $^3\text{He}/^4\text{He}$  ratios ( $R > 10$ ) show moderate enrichment of Si and a low enrichment of N, S, and Ca compared to the events with  $^3\text{He}/^4\text{He} < 10$ . Another notable feature in Figure 6 is that a few cases (#38, 46, and 51) exhibit very low heavy ion abundances

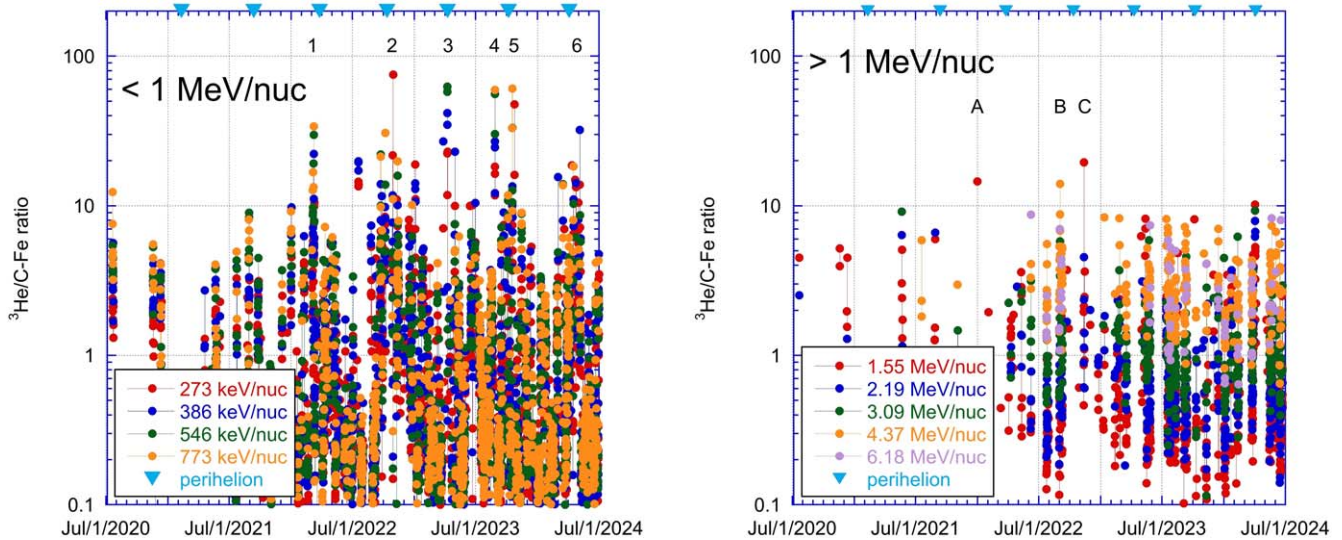


**Figure 7.** Ratio of  $^3\text{He}$  to the sum of C–Fe for 6 hr intervals over the survey period. Left panel: ratios at several energies below 1 MeV per nucleon. The right panel is the same as the left panel but for several energies above 1 MeV nucleon $^{-1}$ . The labeled events (1–5 and A–C) are discussed in the text. Downward triangles mark Solar Orbiter’s perihelia.

with respect to  $^3\text{He}$ . These events overall have an extremely high  $^3\text{He}$  content compared to the heavy ion abundances. We explore this interesting characteristic in the next section, where we perform a separate survey for this particular case of events.

### 3. Events with Extremely High $^3\text{He}/\text{C-Fe}$

A main goal of surveying  $^3\text{He}$ -rich events with the highly sensitive instrumentation of the Solar Orbiter mission is to identify spectral forms that can be compared with models for the events and to provide other constraints that arise from the observations. In this section, we attempt to sample spectra as close as possible to the initial acceleration event and assume that small events with extremely high  $^3\text{He}$  content give the best chance of this. A problem arises: how to characterize high  $^3\text{He}$  content when intensity alone depends on many other factors, such as heliospheric distance and favorable magnetic connection, that are unrelated to the acceleration process itself? An additional serious complication is that in the energy range below  $\sim 1\text{--}2$  MeV nucleon $^{-1}$ , where the spectra are sampled presumably near the “original” state, there are often significant intensities of protons and  $^4\text{He}$  that arise from other sources, such as corotating interaction regions and decay phases of SEP events and interplanetary shocks. Thus, the traditional measure for identifying  $^3\text{He}$ -rich events, namely, the  $^3\text{He}/^4\text{He}$  ratio, is often largely meaningless since the  $^4\text{He}$  arises from different physical mechanisms (e.g., discussions in G. M. Mason et al. 2024).

A recent survey (G. M. Mason et al. 2024) of 34 events observed on Solar Orbiter has shown that  $^3\text{He}$  enrichments were in all cases accompanied by enhancements of Fe whose spectra were clearly related to the  $^3\text{He}$  spectrum. Other heavy ions over the mass range C–Ca were found to be similar in shape to the Fe spectrum. This suggests measuring the  $^3\text{He}$  with respect to heavy ions C–Fe as an identifying device, thus improving statistical accuracy for the heavy ions and avoiding the problems with multiple sources of  $^4\text{He}$  (see S. T. Hart et al. 2024). Figure 7 shows a survey of the Solar Orbiter mission data set of 6 hr averages of the ratio of  $^3\text{He}$  to the sum of C–Fe in several energy bins. The left panel of the figure shows the

energy range below 1 MeV nucleon $^{-1}$ , and the right panel shows the range 1–6 MeV nucleon $^{-1}$ . All time periods are in the plot, including large SEP events, interplanetary shocks, and corotating interaction regions. Six periods with the highest  $^3\text{He}/\text{C-Fe}$  ratios in the range below 1 MeV nucleon $^{-1}$  are marked in the left panel. Each period showed a high ratio for several 6 hr intervals, and in the different events, the high values occurred in several different energy bins in the range below 1 MeV nucleon $^{-1}$ . The period marked with an asterisk had accompanying shock activity and was discarded, leaving events 1–5 to be discussed below. Triangles on the top axis of the figure mark the times of Solar Orbiter perihelia, and the events with high  $^3\text{He}/\text{C-Fe}$  tend to be associated with these intervals, showing the importance of observations closer to the Sun in sampling these low-intensity events.

Comparing the left and right panels in Figure 7, it is apparent that the extreme enrichments seen at lower energies are not observed at higher energies. The three single 6 hr periods with  $^3\text{He}/\text{C-Fe}$  well above 10 in the right panel are from (A) a  $^3\text{He}$ -rich event on 2021 December 31 (event #9 in G. M. Mason et al. 2024), (B) an event with high background in the  $^3\text{He}$  region during the intense interplanetary shock on 2022 September 2, and (C) a period on 2022 November 12 during a multiday period of  $^3\text{He}$  enrichment. We restrict our discussion below to events 1–5 in the left panel since they were for multiple intervals and were the highest ratio values in the survey.

Table 1 lists the properties of the five events, calculated from the spectra averaged over each event. The third and fourth rows list the event start time and duration of the interval used for computing spectra. The time periods of events E1, E3, E4, and E5 were adjusted so that the spectra were summed over periods adjusted for particle energy in order to isolate the  $^3\text{He}$ -rich event from other activity (e.g., G. M. Mason et al. 2000, 2024). The fifth row lists the maximum value of  $^3\text{He}/\text{C-Fe}$  observed in the spectrum of each event, and the sixth row lists the energy bin for which the  $^3\text{He}/\text{C-Fe}$  ratio was at a maximum. In order to compare the  $^3\text{He}$  enrichment in the events selected here with other work, we computed the  $^3\text{He}/\text{C-Fe}$  ratio for a recent survey of 34  $^3\text{He}$ -rich events (G. M. Mason et al. 2024). The average  $^3\text{He}/\text{C-Fe}$  ratio for the 34 events near



**Table 1**  
Properties of Events with Extremely High  $^3\text{He}/\text{C-Fe}$

Event No.	E1	E2	E3	E4	E5
Date	30 Oct 2022	8 Apr 2023	27 Aug 2023	24 Oct 2023	5 May 2024
Start time	0:22	18:00	1:07	18:00	3:56
Length <sup>a</sup> (hr)	16.22 <sup>*</sup>	12.00	42.09 <sup>*</sup>	34.78 <sup>*</sup>	29.63 <sup>*</sup>
Max $^3\text{He}/\text{C-Fe}$	$61.8 \pm 8.0$	$57.4 \pm 10.1$	$45.4 \pm 9.1$	$25.5 \pm 3.6$	$55.6 \pm 17.0$
$E_{\text{max}}$ (MeV/n)	0.386	0.546	0.773	0.273	0.546
$E_0$ $^3\text{He}$	$0.064 \pm 0.002$	$0.166 \pm 0.004$	$0.281 \pm 0.007$	$0.116 \pm 0.004$	$0.369 \pm 0.013$
$E_0$ C-Fe	$0.036 \pm 0.001$	$0.055 \pm 0.002$	$0.102 \pm 0.004$	$0.048 \pm 0.002$	$0.133 \pm 0.012$
$(E_0 \text{ } ^3\text{He})/(E_0 \text{ C-Fe})$	1.78	3.02	2.75	2.40	2.77
SIS-a/-b ratio <sup>b</sup>	$400 \pm 142$	$5.2 \pm 0.8$	$2.7 \pm 0.1$	$4.4 \pm 1.4$	$14.1 \pm 4.6$
e- <sup>c</sup>	y	...	y?	...	y?
$R^d$	0.47	0.29	0.73	0.48	0.65
Lat. <sup>d</sup>	7.66	-4.39	-2.88	7.72	7.77
Angle <sup>e</sup>	-36.85	55.03	154.03	-29.91	165.21
Table A.1 event	23	38	46	51	57
Notes	f	g	g	Si-S rich	...

**Notes.**

<sup>a</sup> An asterisk denotes that the time interval is adjusted for differing particle energies (see text).

<sup>b</sup> Ratio of SIS-a (sunward-looking)/SIS-b (antisunward-looking)  $^3\text{He}$  spectra.

<sup>c</sup> One or more electron injections seen at  $\sim 10\text{--}100$  keV nucleon<sup>-1</sup>.

<sup>d</sup> Heliocentric distance (au) and heliographic latitude (deg).

<sup>e</sup> Separation angle (deg) with respect to Earth; negative is east of Earth-Sun line, and positive is west.

<sup>f</sup> Event 1 occurred during long-term connection interval #20 and event 2 in interval #30 of A. Kouloumvakos et al. (2023).

<sup>g</sup> Event in study of G. M. Mason et al. (2023b, 2024).

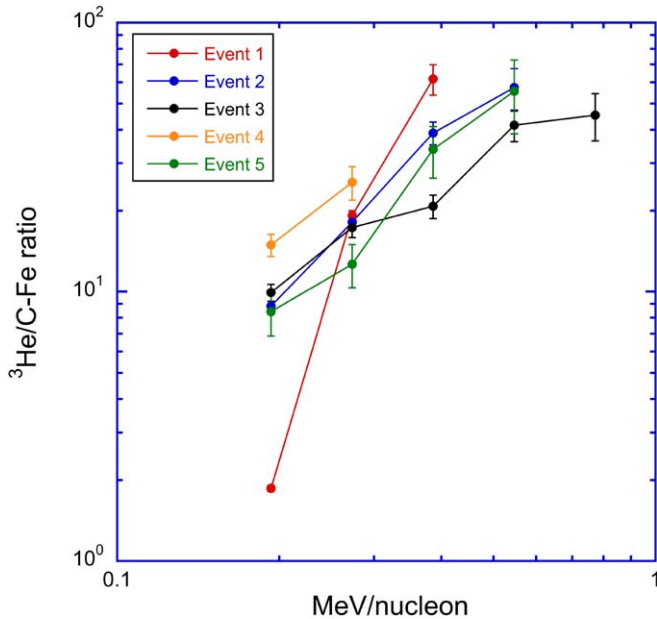


**Figure 8.**  $^3\text{He}/\text{C-Fe}$  ratio as a function of energy for the spectra in Figure 9.

$0.5 \text{ MeV nucleon}^{-1}$  was 4.7, so the events selected here have a factor of 5–13 higher value for this ratio even in events already enriched in  $^3\text{He}$ . The seventh through ninth rows list properties of the spectra discussed below. The tenth row shows the ratio of the SIS-a (sunward) to SIS-b (antisunward) intensity spectra of  $^3\text{He}$ . The eleventh row notes whether electrons of tens of keV were injected in association with each event. The twelfth through fourteenth rows show the location of the spacecraft at the time of the event.

Figure 8 shows the  $^3\text{He}/\text{C-Fe}$  ratios for each event at different energies. The ratios increase sharply with increasing

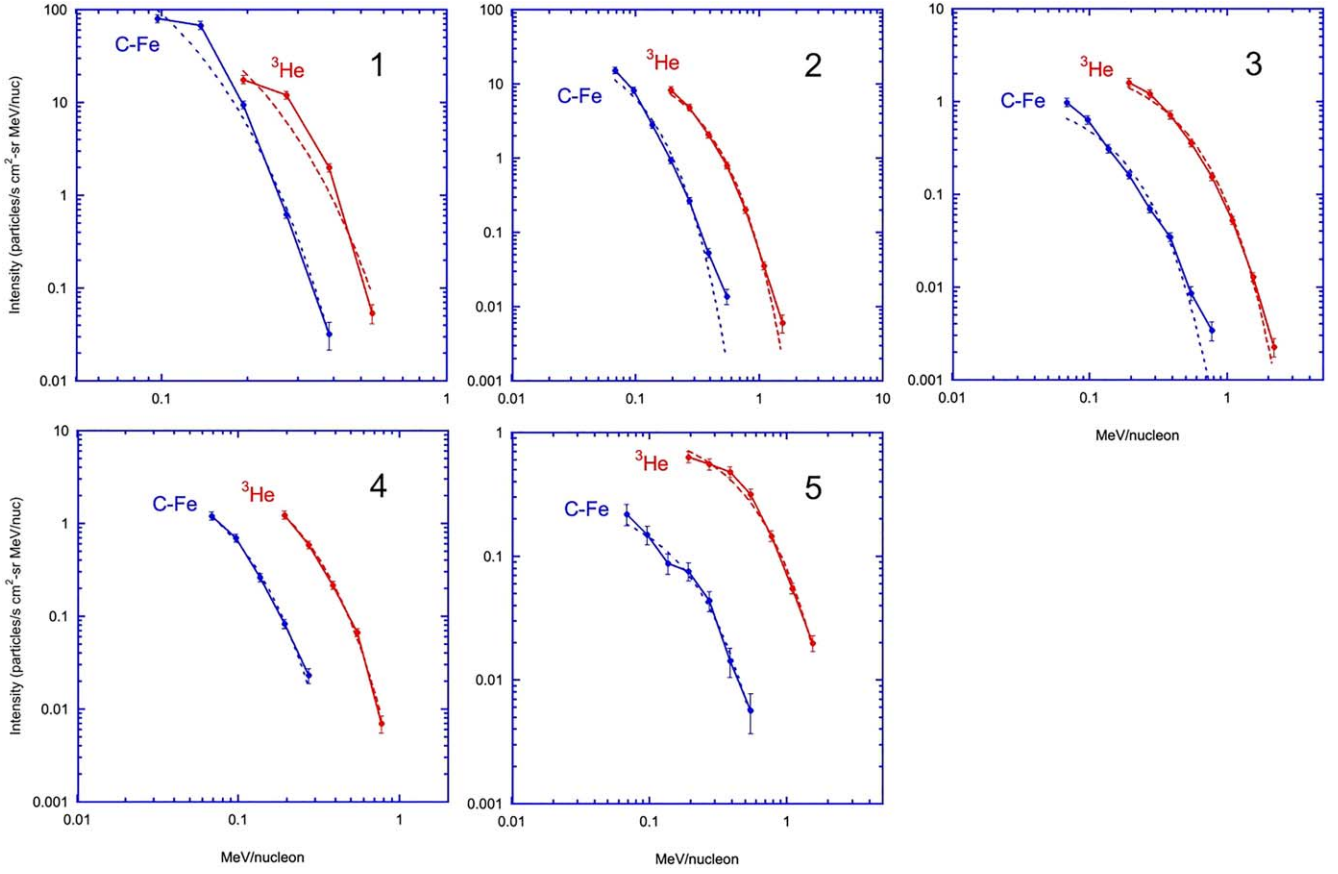
energy due to the difference in spectral shape of  $^3\text{He}$  versus C-Fe, wherein the C-Fe spectra roll over at lower energies than  $^3\text{He}$ . The large variation of these ratios with energy shows the difficulty of identifying these events with too narrow a criterion, e.g., a ratio value at a specific energy per nucleon.

Figure 9 shows  $^3\text{He}$  and C-Fe spectra for each event. An important feature of the figure is that in all cases, the  $^3\text{He}$  spectra show a distinctive curved shape seen in many previous studies cited earlier. However, there was no requirement regarding spectral shape in our selection (e.g., in contrast to G. M. Mason et al. 2024), so this property is a key feature of the high  $^3\text{He}$  content events. The C-Fe spectrum in each of the events is also clearly curved and displaced to lower energies than the  $^3\text{He}$ . Each of the figures shows simple exponential fits  $dJ/dE = C \exp(-E/E_0)$ , where  $C$  is a constant and  $E$  and the rollover energy  $E_0$  are in MeV nucleon<sup>-1</sup> (D. C. Ellison & R. Ramaty 1985; G. M. Mason et al. 2024). The derived rollover energies  $E_0$  for  $^3\text{He}$  and C-Fe are listed in Table 1. Although not ideal, the fits give a simple analytic characterization of the spectra.

The ratio of the rollover energies  $(E_0 \text{ } ^3\text{He})/(E_0 \text{ C-Fe})$  are shown in the ninth row of Table 1. They cover the range 1.78–3.02, with an average value of  $\sim 2.5$ . Figure 10 plots the rollover energy  $(E_0 \text{ C-Fe})$  versus  $(E_0 \text{ } ^3\text{He})$ , with each point labeled corresponding to the event number. There is surprisingly little scatter around the simple linear fit, which has a slope of  $0.33 \pm 0.01$  and a regression coefficient of 0.99. The slope is consistent with the energy shift factor of  $3.0 \pm 1.3$  for  $^3\text{He}$  versus Fe found in a larger survey by G. M. Mason et al. (2024).

#### 4. Discussion

From a survey of SEP data from the Solar Orbiter SIS instrument, we compiled a catalog of 57  $^3\text{He}$ -rich events



**Figure 9.** Differential intensity spectra for  $^3\text{He}$  and the sum of C–Fe for events 1–5 in Figure 7 and Table 1.

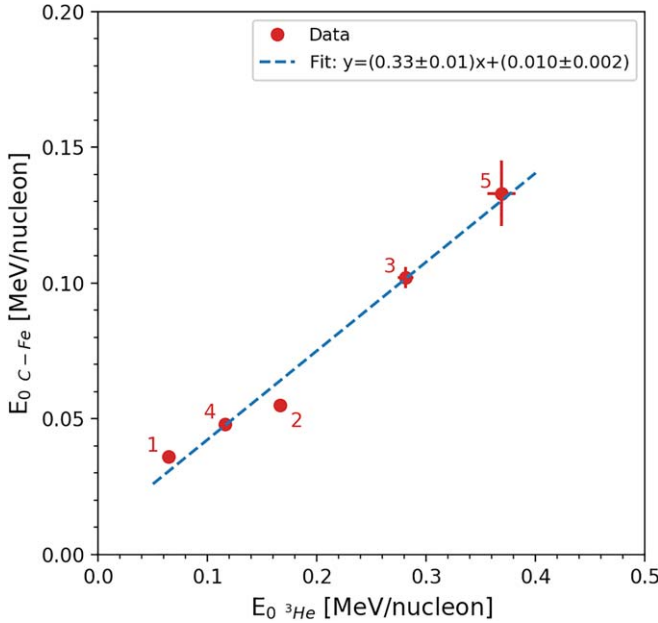


**Figure 10.** Exponential rollover energy for C–Fe spectra vs.  $^3\text{He}$  spectra for the five events in Table 1, with event numbers shown. The dotted line is a linear fit.

with  $^3\text{He}/^4\text{He} > 1$ . This survey covers almost 52 months (4.33 yr) of Solar Orbiter observations, so SIS observed  $\sim 0.8$  events month $^{-1}$  ( $\sim 9.6$  events yr $^{-1}$ ) during the ascending phase of solar cycle 25 in a range of distances below 1 au, with 21 cases being observed below 0.5 au. From the  $^3\text{He}$  fluence

characteristics, we found that many events have very low fluences so that they would be poorly measured or not measured at all by instruments at 1 au.

From the analysis of the composition characteristics of the events, we found that the maximum  $^3\text{He}/^4\text{He}$  ratios are typically observed at  $\sim 0.55$  MeV nucleon $^{-1}$ , and half of the events are distributed within  $2.1 \leq ^3\text{He}/^4\text{He} \leq 6.1$ . From the comparison of the maximum  $^3\text{He}/^4\text{He}$  ratios with those at  $\sim 0.39$  MeV nucleon $^{-1}$ , which is an energy typically used in previous studies, we found that the maximum ratio is on average  $\sim 2$  times higher. This difference arises from an energy dependence in the abundance ratios that was not accounted for systematically in earlier studies. We also showed that there are nine events that exhibit extremely high maximum  $^3\text{He}/^4\text{He}$  ratios ( $>10$ ). Such large ratios have rarely been reported in past studies (G. M. Mason et al. 2002; G. C. Ho et al. 2005). From the analysis of the maximum Fe/O abundance ratios, we showed that the events exhibit typical values of impulsive SEPs. We also analyzed the  $^3\text{He}/\text{H}$  ratios, and we found that on average the ratio is  $\sim 0.5$ , which is extremely high considering that the  $^3\text{He}/\text{H}$  in the solar wind is approximately  $10^{-4}$ . A striking feature is that eight cases were found with maximum  $^3\text{He}/\text{H} > 1$ . Events with  $^3\text{He}/\text{H} > 1$  have been reported only rarely (R. Bučík et al. 2021; G. M. Mason et al. 2023b). The high background H fluxes in most cases made it difficult to further explore the characteristics of  $^3\text{He}/\text{H}$ , but it seems that most of the events that exhibit extremely high  $^3\text{He}/^4\text{He}$  ratios also have  $^3\text{He}/\text{H} > 1$ .

We also examined the  $^3\text{He}/^4\text{He}$  and Fe/O abundance ratios as a function of energy. This analysis showed that the  $^3\text{He}/^4\text{He}$



ratio clearly increases with energy, especially for events with high  $^3\text{He}/^4\text{He}$  ratios, whereas for the Fe/O ratio, there is no dependence with energy in any case. A similar energy dependence of the  $^3\text{He}/^4\text{He}$  ratio with peaks at around 1 MeV nucleon $^{-1}$  has been presented by G. M. Mason et al. (2002) for their “class 2” events that exhibit curved  $^3\text{He}$  and Fe spectra and high  $^3\text{He}/^4\text{He}$  ratios. Analyzing further the heavy ion abundances normalized to  $^3\text{He}$  at  $\sim 0.19$  MeV nucleon $^{-1}$ , for events with extremely high  $^3\text{He}/^4\text{He}$  ratios ( $\geq 10$ ), we found that most cases exhibit moderate enrichment of Si and a low enrichment of N, S, and Ca compared to the events with  $^3\text{He}/^4\text{He}$  ratios  $< 10$ . We also found that there are a few interesting cases that exhibit an extremely high  $^3\text{He}$  content compared to the heavy ion abundances. We found this to be an interesting characteristic, and we have further analyzed this particular case of events.

Exploring this aspect further, we have surveyed 52 months of observations with the Solar Orbiter spacecraft to identify  $^3\text{He}$ -rich SEP events with extremely large enhancements of  $^3\text{He}$ . Such large enhancements of  $^3\text{He}$  in many small solar flare events have been known for a long time. In the energy range below  $\sim 1$  MeV nucleon $^{-1}$ , five events were found with  $^3\text{He}/\text{C-Fe}$  ratios in the range 25–62, a factor of  $\sim 1500$  higher than in the slow solar wind (R. Bodmer et al. 1995; G. Gloeckler et al. 1998; R. von Steiger et al. 2000). From the analysis of this particular class, we found the following.

1. Curved  $^3\text{He}$  and heavy nuclei spectra are both present in all cases: they roll over at higher energies and flatten toward low energy.
2. The spectral form can be reasonably fit with simple exponentials, where  $^3\text{He}$  rollover energy is in the range of a few hundred keV per nucleon, and the C–Fe rollover energy is  $\sim 2$ –3 times lower.

3. These differences in spectral rollover energy lead to a strong energy dependence of the ratio  $^3\text{He}/\text{C-Fe}$ , rising sharply with energy.
4. These features were not observed for particles above  $\sim 1$  MeV nucleon $^{-1}$ .

We believe that for the events with extremely high  $^3\text{He}/\text{C-Fe}$  ratios, the high value is due to differences in spectral shape above the rollover energy, wherein the  $^3\text{He}$  rolls over at higher energy than the other species. The most extreme enhancements are found in small events where the  $^3\text{He}$  maximum energy is below  $\sim 1$  MeV nucleon $^{-1}$ , and it remains unclear why events with higher maximum energies do not exhibit this behavior. Many of these features are seen in the plasma-wave turbulence models of S. Liu et al. (2004, 2006), but other models may be capable of producing them as well (I. Roth & M. Temerin 1997; J. F. Drake et al. 2009; A. Fitzmaurice et al. 2024).

### Acknowledgments

Solar Orbiter is a mission of international cooperation between ESA and NASA, operated by ESA. The Suprathermal Ion Spectrograph (SIS) is a European facility instrument funded by ESA under contract number SOL.ASTR.CON.00004. We thank ESA and NASA for their support of the Solar Orbiter. Solar Orbiter postlaunch work at JHU/APL and the Southwest Research Institute is supported by NASA contract NNN06AA01C and at CAU by German Space Agency (DLR) grant #50OT2002. J.R.P. has been funded by MICIU/AEI and FEDER, UE under project PID2023-150952OB-I00/10.13039/501100011033.

### Appendix

This appendix provides supplementary data relevant to the study. Table A1 lists the 57 events identified in our survey. For each event, we provide the properties used in the statistical analysis (see main text for a detailed description of the table).

**Table A1**  
List of  $^3\text{He}$ -rich Events from SIS Data Survey

Event	Date	$T_S$	$r_{\text{sc}}$ (au)	$(^{a,b})F_{^3\text{He}}$ $\times 10^{-3}$	$(^{a,b})F_{^4\text{He}}$ $\times 10^{-3}$	$^3\text{He}/^4\text{He}$			Fe/O			$^3\text{He}/\text{H}$ Max <sup>(c)</sup>
						$E^{(b)}$	Max <sup>(c)</sup>	$E_{\text{Max}}^{(d)}$	$E^{(b)}$	Max <sup>(c)</sup>	$E_{\text{Max}}^{(d)}$	
(1)	(2)	(3)	(4)	(5)	(6)	(7)	(8)	(9)	(10)	(11)	(12)	(13)
1	2020-11-17	11:00	0.93	18.1 $\pm$ 0.9	24.1 $\pm$ 1.1	0.7 $\pm$ 0.1	3.2 $\pm$ 0.7	1.1	0.6 $\pm$ 0.2	1.1 $\pm$ 0.2	0.3	0.28 $\pm$ 0.07
2	2021-02-13	12:00	0.50	1.9 $\pm$ 0.3	0.4 $\pm$ 0.1	4.8 $\pm$ 1.8	4.8 $\pm$ 1.8	0.4	...	1.6 $\pm$ 0.8	0.1	0.44 $\pm$ 0.12
3	2021-04-24	13:00	0.87	4.6 $\pm$ 0.5	...	...	6.3 $\pm$ 1.8	0.3	...	...	...	0.47 $\pm$ 0.12
4	2021-05-21	22:00	0.94	88.8 $\pm$ 2.1	105.3 $\pm$ 2.3	0.8 $\pm$ 0.0	3.9 $\pm$ 1.1	2.2	0.6 $\pm$ 0.1	0.7 $\pm$ 0.3	1.5	0.22 $\pm$ 0.04
5	2021-09-06	14:00	0.59	1.2 $\pm$ 0.2	0.5 $\pm$ 0.2	2.3 $\pm$ 0.8	2.3 $\pm$ 0.8	0.4	...	...	...	0.21 $\pm$ 0.07
6	2021-10-28	05:00	0.80	1.3 $\pm$ 0.3	...	...	3.5 $\pm$ 1.2	0.3	...	...	...	0.49 $\pm$ 0.16
7	2021-12-20	07:00	1.01	2.6 $\pm$ 0.4	1.5 $\pm$ 0.3	1.7 $\pm$ 0.4	2.1 $\pm$ 0.7	0.5	...	1.3 $\pm$ 0.6	0.1	0.02 $\pm$ 0.00
8	2021-12-31	12:30	1.00	75.0 $\pm$ 1.9	32.1 $\pm$ 1.3	2.3 $\pm$ 0.1	20.4 $\pm$ 4.9	1.1	1.0 $\pm$ 0.1	1.1 $\pm$ 0.1	0.3	0.35 $\pm$ 0.08
9	2022-01-13	18:00	0.96	1.1 $\pm$ 0.2	0.7 $\pm$ 0.2	1.5 $\pm$ 0.5	1.9 $\pm$ 0.8	0.8	...	...	...	0.12 $\pm$ 0.04
10	2022-02-05	12:00	0.82	2.5 $\pm$ 0.4	0.5 $\pm$ 0.2	5.1 $\pm$ 1.8	7.1 $\pm$ 2.9	0.5	...	...	...	0.29 $\pm$ 0.10
11	2022-02-07	10:00	0.80	16.6 $\pm$ 0.9	31.4 $\pm$ 1.3	0.5 $\pm$ 0.0	2.3 $\pm$ 1.0	1.5	0.7 $\pm$ 0.2	1.1 $\pm$ 0.2	0.3	0.07 $\pm$ 0.02
12	2022-03-03	15:00	0.55	42.2 $\pm$ 1.5	4.1 $\pm$ 0.5	10.2 $\pm$ 1.2	11.4 $\pm$ 2.4	0.5	3.9 $\pm$ 0.8	3.9 $\pm$ 1.5	0.5	0.72 $\pm$ 0.04
13	2022-03-06	00:00	0.51	170.3 $\pm$ 2.9	177.6 $\pm$ 3.0	1.0 $\pm$ 0.0	3.3 $\pm$ 0.5	1.5	1.3 $\pm$ 0.2	1.8 $\pm$ 0.2	0.3	0.47 $\pm$ 0.06
14	2022-03-08	12:00	0.49	77.3 $\pm$ 2.0	185.0 $\pm$ 3.0	0.4 $\pm$ 0.0	1.7 $\pm$ 0.5	1.5	0.3 $\pm$ 0.1	0.4 $\pm$ 0.1	0.3	0.01 $\pm$ 0.00
15	2022-03-09	19:00	0.48	14.6 $\pm$ 0.9	10.2 $\pm$ 0.7	1.4 $\pm$ 0.1	5.0 $\pm$ 1.0	0.8	0.5 $\pm$ 0.2	0.7 $\pm$ 0.1	0.1	0.15 $\pm$ 0.03
16	2022-07-18	19:00	1.00	29.5 $\pm$ 1.2	4.0 $\pm$ 0.4	7.3 $\pm$ 0.9	8.8 $\pm$ 1.4	0.5	...	0.7 $\pm$ 0.3	0.1	0.08 $\pm$ 0.00
17	2022-07-21	16:00	0.99	7.3 $\pm$ 0.6	2.4 $\pm$ 0.3	3.1 $\pm$ 0.5	8.5 $\pm$ 3.2	0.8	...	...	...	0.06 $\pm$ 0.01
18	2022-08-18	13:00	0.86	0.6 $\pm$ 0.2	0.3 $\pm$ 0.1	1.7 $\pm$ 0.8	4.0 $\pm$ 1.2	0.2	...	...	...	0.26 $\pm$ 0.07
19	2022-10-27	11:00	0.42	9.0 $\pm$ 0.7	3.3 $\pm$ 0.4	2.7 $\pm$ 0.4	2.7 $\pm$ 0.4	0.4	...	2.7 $\pm$ 0.9	0.1	0.30 $\pm$ 0.03
20	2022-10-29a	02:00	0.45	448.3 $\pm$ 4.7	133.7 $\pm$ 2.6	3.4 $\pm$ 0.1	3.4 $\pm$ 0.1	0.4	1.1 $\pm$ 0.1	1.5 $\pm$ 0.2	0.5	1.35 $\pm$ 0.09
21	2022-10-29b	10:00	0.45	...	...	...	22.0 $\pm$ 4.8	0.5	...	1.1 $\pm$ 0.3	0.5	1.41 $\pm$ 0.20
22	2022-10-29c	16:30	0.45	2.4 $\pm$ 0.3	...	...	10.7 $\pm$ 3.7	0.3	...	1.3 $\pm$ 0.4	0.2	1.66 $\pm$ 0.49
23	2022-10-30	01:30	0.46	29.8 $\pm$ 1.2	0.8 $\pm$ 0.2	37.4 $\pm$ 9.5	37.4 $\pm$ 9.5	0.4	...	1.0 $\pm$ 0.0	0.1	8.29 $\pm$ 1.02
24	2022-11-09	04:00	0.59	4.7 $\pm$ 0.5	6.6 $\pm$ 0.6	0.7 $\pm$ 0.1	1.2 $\pm$ 0.3	0.5	2.7 $\pm$ 0.3	2.7 $\pm$ 0.3	0.4	0.05 $\pm$ 0.01
25	2022-11-14	03:00	0.65	116.7 $\pm$ 2.4	255.6 $\pm$ 3.6	0.5 $\pm$ 0.0	1.1 $\pm$ 0.6	3.1	1.0 $\pm$ 0.1	1.7 $\pm$ 0.1	0.1	0.12 $\pm$ 0.01
26	2022-12-16	00:00	0.90	10.4 $\pm$ 0.7	3.7 $\pm$ 0.4	2.8 $\pm$ 0.4	2.9 $\pm$ 0.7	0.8	...	1.1 $\pm$ 0.4	0.1	0.11 $\pm$ 0.01
27	2023-01-03	19:00	0.95	20.1 $\pm$ 1.0	15.1 $\pm$ 0.9	1.3 $\pm$ 0.1	1.4 $\pm$ 0.2	0.5	0.9 $\pm$ 0.3	1.6 $\pm$ 0.4	0.3	0.11 $\pm$ 0.01
28	2023-01-22a	00:30	0.94	8.4 $\pm$ 0.6	14.6 $\pm$ 0.9	0.6 $\pm$ 0.1	1.8 $\pm$ 0.6	1.1	0.5 $\pm$ 0.2	0.9 $\pm$ 0.2	0.2	0.01 $\pm$ 0.00
29	2023-01-22b	16:00	0.94	21.9 $\pm$ 1.0	13.7 $\pm$ 0.8	1.6 $\pm$ 0.1	2.4 $\pm$ 0.5	0.8	0.6 $\pm$ 0.2	0.9 $\pm$ 0.1	0.2	0.04 $\pm$ 0.00
30	2023-01-25	12:00	0.94	12.1 $\pm$ 0.8	16.3 $\pm$ 0.9	0.7 $\pm$ 0.1	1.1 $\pm$ 0.1	0.2	0.3 $\pm$ 0.1	1.6 $\pm$ 0.2	0.1	0.17 $\pm$ 0.01
31	2023-01-27	06:00	0.93	5.4 $\pm$ 0.5	2.0 $\pm$ 0.3	2.7 $\pm$ 0.5	6.8 $\pm$ 2.2	0.5	...	1.8 $\pm$ 0.6	0.2	0.68 $\pm$ 0.18
32	2023-03-04	12:00	0.71	1.3 $\pm$ 0.3	0.7 $\pm$ 0.2	1.8 $\pm$ 0.6	1.8 $\pm$ 0.6	0.4	...	...	...	0.08 $\pm$ 0.02
33	2023-03-05	04:00	0.70	2.8 $\pm$ 0.4	7.1 $\pm$ 0.6	0.4 $\pm$ 0.1	1.2 $\pm$ 0.5	1.5	...	...	...	0.05 $\pm$ 0.02
34	2023-03-28	00:00	0.41	15.1 $\pm$ 0.9	4.2 $\pm$ 0.5	3.6 $\pm$ 0.4	4.7 $\pm$ 0.8	0.5	...	1.1 $\pm$ 0.3	0.1	0.03 $\pm$ 0.00
35	2023-03-29	11:30	0.40	1.1 $\pm$ 0.2	0.4 $\pm$ 0.1	2.9 $\pm$ 1.2	2.9 $\pm$ 1.2	0.4	...	...	...	0.11 $\pm$ 0.03
36	2023-03-30	00:00	0.39	1.8 $\pm$ 0.3	...	...	4.0 $\pm$ 1.4	0.3	...	...	...	0.15 $\pm$ 0.03
37	2023-04-08a	06:00	0.30	2.1 $\pm$ 0.3	...	...	3.1 $\pm$ 0.8	0.3	...	...	...	1.18 $\pm$ 0.39
38	2023-04-08b	20:00	0.30	93.7 $\pm$ 2.2	16.6 $\pm$ 0.9	5.7 $\pm$ 0.3	21.7 $\pm$ 5.7	0.8	...	2.1 $\pm$ 0.7	0.3	2.55 $\pm$ 0.34
39	2023-04-15	05:00	0.31	...	...	...	4.9 $\pm$ 1.7	0.3	...	...	...	0.44 $\pm$ 0.11
40	2023-04-16	07:00	0.32	0.9 $\pm$ 0.2	...	...	12.8 $\pm$ 3.8	0.2	...	...	...	...
41	2023-05-01	11:00	0.51	11.0 $\pm$ 0.7	6.3 $\pm$ 0.6	1.7 $\pm$ 0.2	1.7 $\pm$ 0.2	0.4	...	0.5 $\pm$ 0.2	0.1	0.02 $\pm$ 0.00
42	2023-06-13	09:00	0.89	1.8 $\pm$ 0.3	...	...	2.4 $\pm$ 0.7	0.3	...	1.0 $\pm$ 0.4	0.1	0.17 $\pm$ 0.04
43	2023-06-28	19:00	0.94	10.0 $\pm$ 0.7	13.7 $\pm$ 0.8	0.7 $\pm$ 0.1	1.2 $\pm$ 0.3	1.1	1.1 $\pm$ 0.4	2.4 $\pm$ 1.1	0.5	0.23 $\pm$ 0.04
44	2023-06-30	03:00	0.95	9.3 $\pm$ 0.7	4.0 $\pm$ 0.4	2.3 $\pm$ 0.3	2.5 $\pm$ 0.4	0.5	...	1.4 $\pm$ 0.3	0.1	0.29 $\pm$ 0.02
45	2023-07-07	20:00	0.95	5.1 $\pm$ 0.5	2.7 $\pm$ 0.4	1.9 $\pm$ 0.3	3.3 $\pm$ 0.8	0.5	0.5 $\pm$ 0.2	2.4 $\pm$ 0.9	0.2	0.13 $\pm$ 0.02
46	2023-08-27	09:30	0.74	88.1 $\pm$ 2.1	4.9 $\pm$ 0.5	17.8 $\pm$ 1.8	49.3 $\pm$ 12.9	0.8	1.0 $\pm$ 0.4	2.9 $\pm$ 1.0	0.3	1.41 $\pm$ 0.40

**Table A1**  
(Continued)

Event	Date	$T_S$	$r_{sc}$ (au)	$(^{a,b})F_{^3\text{He}}$ $\times 10^{-3}$	$(^{a,b})F_{^4\text{He}}$ $\times 10^{-3}$	$^3\text{He}/^4\text{He}$			Fe/O			$^3\text{He}/\text{H}$
						$E^{(b)}$	Max $^{(c)}$	$E_{\text{Max}}^{(d)}$	$E^{(b)}$	Max $^{(c)}$	$E_{\text{Max}}^{(d)}$	Max $^{(c)}$
(1)	(2)	(3)	(4)	(5)	(6)	(7)	(8)	(9)	(10)	(11)	(12)	(13)
47	2023-08-29	00:00	0.72	2.3 $\pm$ 0.3	...	...	2.4 $\pm$ 0.7	0.3	...	...	...	0.12 $\pm$ 0.02
48	2023-10-05	04:30	0.30	25.0 $\pm$ 1.1	15.0 $\pm$ 0.9	1.7 $\pm$ 0.1	5.8 $\pm$ 1.8	1.1	0.4 $\pm$ 0.1	0.5 $\pm$ 0.2	0.1	0.04 $\pm$ 0.00
49	2023-10-07	01:30	0.29	1.3 $\pm$ 0.3	0.5 $\pm$ 0.2	2.6 $\pm$ 1.0	2.9 $\pm$ 1.2	0.3	...	...	...	0.04 $\pm$ 0.01
50	2023-10-19	09:00	0.39	4.7 $\pm$ 0.5	4.2 $\pm$ 0.5	1.1 $\pm$ 0.2	1.6 $\pm$ 0.4	0.5	...	0.8 $\pm$ 0.3	0.2	0.05 $\pm$ 0.02
51	2023-10-24	22:00	0.46	18.7 $\pm$ 1.0	...	...	22.7 $\pm$ 4.1	0.3	...	0.9 $\pm$ 0.5	0.1	1.44 $\pm$ 0.15
52	2023-11-09	05:30	0.66	1.4 $\pm$ 0.3	...	...	2.1 $\pm$ 0.9	0.2	...	...	...	0.22 $\pm$ 0.06
53	2023-11-14	06:00	0.71	28.2 $\pm$ 1.2	22.9 $\pm$ 1.1	1.2 $\pm$ 0.1	3.0 $\pm$ 0.6	1.5	1.2 $\pm$ 0.3	1.3 $\pm$ 0.3	0.3	0.28 $\pm$ 0.07
54	2023-12-22	18:00	0.94	2.1 $\pm$ 0.3	2.4 $\pm$ 0.3	0.9 $\pm$ 0.2	1.3 $\pm$ 0.6	1.1	...	...	...	0.02 $\pm$ 0.00
55	2024-04-11	17:00	0.33	3.0 $\pm$ 0.4	1.4 $\pm$ 0.3	2.1 $\pm$ 0.5	2.4 $\pm$ 0.3	0.3	...	1.7 $\pm$ 0.3	0.1	0.54 $\pm$ 0.07
56	2024-04-21	09:00	0.46	5.8 $\pm$ 0.5	4.1 $\pm$ 0.5	1.4 $\pm$ 0.2	3.1 $\pm$ 0.9	0.5	...	1.1 $\pm$ 0.3	0.1	0.20 $\pm$ 0.06
57	2024-05-05	08:00	0.64	21.2 $\pm$ 1.0	8.3 $\pm$ 0.6	2.6 $\pm$ 0.2	6.0 $\pm$ 1.5	1.1	...	1.4 $\pm$ 0.6	0.2	0.52 $\pm$ 0.15

**Notes.**

<sup>a</sup> Fluence in particles/(cm<sup>2</sup> sr MeV nucleon<sup>-1</sup>).

<sup>b</sup> Calculated in 320.0–452.5 keV nucleon<sup>-1</sup> energy range.

<sup>c</sup> Maximum abundance ratio.

<sup>d</sup> Energy of the maximum abundance ratio in MeV nucleon<sup>-1</sup>.



## ORCID iDs

A. Kouloumvakos  <https://orcid.org/0000-0001-6589-4509>  
 G. M. Mason  <https://orcid.org/0000-0003-2169-9618>  
 G. C. Ho  <https://orcid.org/0000-0003-1093-2066>  
 R. C. Allen  <https://orcid.org/0000-0003-2079-5683>  
 J. Rodriguez-Pacheco  <https://orcid.org/0000-0002-4240-1115>  
 R. F. Wimmer-Schweingruber  <https://orcid.org/0000-0002-7388-173X>

## References

- Anglin, J. D. 1975, *ApJ*, **198**, 733  
 Balasubrahmanyam, V. K., & Serlemitsos, A. T. 1974, *Natur*, **252**, 460  
 Bodmer, R., Bochsler, P., Geiss, J., von Steiger, R., & Gloeckler, G. 1995, *SSRv*, **72**, 61  
 Broaden, A., Zhang, T. X., Edwards, V. M., et al. 2013, *JASTP*, **97**, 22  
 Bučík, R. 2020, *SSRv*, **216**, 24  
 Bučík, R., Mason, G. M., Gómez-Herrero, R., et al. 2021, *A&A*, **656**, L11  
 Bučík, R., Mason, G. M., Nitta, N. V., et al. 2023, *A&A*, **673**, L5  
 Desai, M. I., Mason, G. M., Gold, R. E., et al. 2006, *ApJ*, **649**, 470  
 Drake, J. F., Cassak, P. A., Shay, M. A., Swisdak, M., & Quataert, E. 2009, *ApJL*, **700**, L16  
 Ellison, D. C., & Ramaty, R. 1985, *ApJ*, **298**, 400  
 Fisk, L. A. 1978, *ApJ*, **224**, 1048  
 Fitzmaurice, A., Drake, J. F., & Swisdak, M. 2024, *ApJ*, **964**, 97  
 Garrard, T. L., Stone, E. C., & Vogt, R. E. 1973, *NASSP*, **342**, 341  
 Gary, S. P. 1993, *Theory of Space Plasma Microinstabilities* (Cambridge: Cambridge Univ. Press)  
 Gloeckler, G., Cain, J., Ipavich, F. M., et al. 1998, *SSRv*, **86**, 497  
 Hart, S. T., Dayeh, M. A., Bučík, R., et al. 2022, *ApJS*, **263**, 22  
 Hart, S. T., Dayeh, M. A., Bučík, R., et al. 2024, *ApJ*, **974**, 220  
 Ho, G. C., Mason, G. M., Allen, R. C., et al. 2022, *FrASS*, **9**, 939799  
 Ho, G. C., Roelof, E. C., & Mason, G. M. 2005, *ApJL*, **621**, L141  
 Hsieh, K. C., & Simpson, J. A. 1970, *ApJL*, **162**, L191  
 Kocharov, L. G., & Kocharov, G. E. 1984, *SSRv*, **38**, 89  
 Kouloumvakos, A., Mason, G. M., Ho, G. C., et al. 2023, *ApJ*, **956**, 123  
 Lario, D., Aran, A., Gómez-Herrero, R., et al. 2013, *ApJ*, **767**, 41  
 Li, T. M., Li, C., Ding, W. J., & Chen, P. F. 2021, *ApJ*, **922**, 50  
 Liu, S., Petrosian, V., & Mason, G. M. 2004, *ApJL*, **613**, L81  
 Liu, S., Petrosian, V., & Mason, G. M. 2006, *ApJ*, **636**, 462  
 Mason, G. M. 2007, *SSRv*, **130**, 231  
 Mason, G. M., Dwyer, J. R., & Mazur, J. E. 2000, *ApJL*, **545**, L157  
 Mason, G. M., Kouloumvakos, A., Ho, G. C., et al. 2024, *ApJ*, **974**, 54  
 Mason, G. M., Mazur, J. E., Dwyer, J. R., et al. 2004, *ApJ*, **606**, 555  
 Mason, G. M., Nitta, N. V., Bučík, R., et al. 2023a, *A&A*, **669**, L16  
 Mason, G. M., Nitta, N. V., Wiedenbeck, M. E., & Innes, D. E. 2016, *ApJ*, **823**, 138  
 Mason, G. M., Roth, I., Nitta, N. V., et al. 2023b, *ApJ*, **957**, 112  
 Mason, G. M., Wiedenbeck, M. E., Miller, J. A., et al. 2002, *ApJ*, **574**, 1039  
 Miller, J. A. 1998, *SSRv*, **86**, 79  
 Miller, J. A. 2000, in *IAU Symp.* 195, *Highly Energetic Physical Processes and Mechanisms for Emission from Astrophysical Plasmas*, ed. P. C. H. Martens, S. Tsuruta, & M. A. Weber (Cambridge: Cambridge Univ. Press), 277  
 Müller, D., St. Cyr, O. C., Zouganelis, I., et al. 2020, *A&A*, **642**, A1  
 Paesold, G., Kallenbach, R., & Benz, A. O. 2003, *ApJ*, **582**, 495  
 Reames, D. V. 1995, *AdSpR*, **15**, 41  
 Reames, D. V. 2021, *SSRv*, **217**, 72  
 Rodríguez-García, L., Gómez-Herrero, R., Dresing, N., et al. 2023, *A&A*, **670**, A51  
 Rodríguez-Pacheco, J., Wimmer-Schweingruber, R. F., Mason, G. M., et al. 2020, *A&A*, **642**, A7  
 Roth, I. 2006, *AdSpR*, **38**, 75  
 Roth, I., & Temerin, M. 1997, *ApJ*, **477**, 940  
 Serlemitsos, A. T., & Balasubrahmanyam, V. K. 1975, *ApJ*, **198**, 195  
 Stix, T. H. 1992, *Waves in Plasmas* (New York: American Institute of Physics)  
 Temerin, M., & Roth, I. 1992, *ApJL*, **391**, L105  
 von Steiger, R., Schwadron, N. A., Fisk, L. A., et al. 2000, *JGR*, **105**, 27217  
 Wimmer-Schweingruber, R. F., Janitzek, N. P., Pacheco, D., et al. 2021, *A&A*, **656**, A22  
 Zhang, T. X. 1995, *ApJ*, **449**, 916  
 Zhang, T. X. 1999, *ApJ*, **518**, 954  
 Zhang, T. X. 2003, *JGRA*, **108**, 1031